JEE Journal of Ecological Engineering

Journal of Ecological Engineering 2023, 24(9), 246–259
https://doi.org/10.12911/22998993/168500
ISSN 2299–8993, License CC-BY 4.0

Received: 2023.05.12
Accepted: 2023.06.18
Published: 2023.07.20

Decontamination of Metronidazole Antibiotic: A Novel Nanocomposite-Based Strategy

Rasha Khalid Sabri Mhemid[1], Liqaa I. Saeed[2], Mohammed Salim Shihab[3*]

[1] Department of Environmental Technologies, College of Environmental Science and Technologies, University of Mosul, 41001, Mosul, Iraq

[2] Department of Mining Engineering, College of Petroleum and Mining Engineering, University of Mosul, 41001, Mosul, Iraq

[3] Department of Environmental Engineering, College of Engineering, University of Mosul, 41001, Mosul, Iraq

* Corresponding author's e-mail: shihab77@uomosul.edu.iq

ABSTRACT

In this study, the synthesis of magnetic nanoparticles (MNPs) employing leaf extract from Alocasiamacrorrhiza was investigated as a reducing agent. $CuFe_2O_4$, $CuFe_2O_4$/CuO, and $CuFe_2O_4$/CuO/CdS made constituted the core-shell of these MNPs, which were stabilized on naturally Ninevite rocks (NRs) to provide a more cost-effective support. Analytical techniques of various methods were used to characterize the MNPs/NR nanocomposite that was produced utilizing eco-friendly methods. Among the methods used were infrared spectroscopy, X-ray diffraction, scanning electron microscopy, and vibrating sample magnetometry (VSM). The antibiotic Metronidazole (MET) was broken down using a potent nanocatalyst made of MNPs in a solar-irradiated batch system. A solar-photocatalytic system was used to investigate the effects of the initial MET concentration, irradiation time, H_2O_2 concentration, catalyst nanocomposite concentration, and pH solution on MET photodegradation. Artificial neural networks (ANNs) were also used in data modeling to determine which oxidation technique performed the best in certain conditions. This investigation showed that the $CuFe_2O_4$/CuO/CdS magnetic catalyst had the greatest MET removal efficiency of 97% among all MNPs. Moreover, ANN were used to examine data from the photocatalytic oxidation of MET utilizing a $CuFe_2O_4$/CuO/CdS/NRs catalyst. The results revealed that the MNP dose had the highest influence on the photodegradation of MET. The correlation coefficients (R^2) for the training regressions, validation, testing, and total data were all 0.999, 0.996, 0.993, and 0.998, respectively.

Keywords: metronidazole antibiotic, magnetic nanoparticles, photodegradation, ninevite rocks, artificial neural network.

INTRODUCTION

Pharmaceutical chemicals, particularly antibiotics, are frequent water pollutants and constitute a major hazard to the ecosystem and human health. (Niaki et al., 2021). Metronidazole (MET), one of the world's most regularly used antibiotics, treats infectious diseases caused by anaerobic bacteria and protozoa. (Forouzesh et al., 2019). Antibiotic wastewater contains more than 100 mg/L (Ingerslev et al., 2001). Standard treatment techniques fail to eliminate MET because it is persistent, non-biodegradable, and very soluble (Sievers, 2011). To preserve the ecology, MET must be removed from contaminated water (Farzadkia et al., 2015). Thus, efficient new MET treatment technologies are necessary. Studies suggest heterogeneous photocatalyst-based advanced oxidation processes (AOPs) can remove MET from wastewater (Wang et al., 2016). Photocatalytic treatment of hazardous substances is one of the most promising alternative processes (AOPs) (Nikravan and Afsoun, 2015). The photocatalytic treatment of MET is examined using ZnO, TiO_2, Ga_2O_3, SnO_2/Co_3O_4, $CoFe_2O_4$, Zn-SnO_3, $BiVO_4$, Fe-doped SnO_2/Co_3O_4, $BiVO_4$/N-rGO, nanozeolites/NiO/SnO_2, $BiVO_4$/$FeVO_4$, and Cu2S/Ag_2S/$BiVO_4$ (Appavu et al., 2018). New

nanobiomagnetic photocatalysts are needed to remove MET from wastewater due to the current catalysts' high cost, biocompatibility, reusability, and stability issues. Magnetic Fenton-type catalysts were proposed in the scientific literature to overcome these issues (Heidari et al., 2019) and (Sharma et al., 2020). Due to their complex structure and several degrees of freedom, ferrites with the general formula MFe_2O_4 (M = Cd, Mn, Cu, Zn, Ni) are more flexible and used in many applications, including photocatalytic degradation (Shi et al., 2012). Catalytic applications have garnered attention for copper ferrites nanoparticles (Verma et al., 2019). CdS/Copper Ferrites core-shell has boosted CdS's stability and photocatalytic activity (Fang et al., 2016). Heterogeneous photocatalysis uses two types of photoreactors: slurry reactors with suspended catalyst particles and reactors with catalysts immobilised on different inert substrates. Photocatalyst recovery and reuse are essential for sustainable process management. (Sulaiman and Alwared, 2022). The sol-gel process is used to create complex material systems and use them as surface coatings on stainless steel, glass slides, glass spheres, beads, Raschig rings, and zeolites. (Sharma et al., 2020). According to Moath H. Mustafa (2011), nivite is a low-cost, silica-rich rock found in the city. Its high porosity, permeability, and surface area (300–800 m^2/g) make it an excellent immobilised pollution removal medium(Salim Q. AL-Naqib, 2006).

To our knowledge, no solar–photocatalytic reactor has utilised various magnetic nanoparticles (MNPs) immobilised on NRs, such as $CuFe_2O_4$, $CuFe_2O_4$/CuO, and $CuFe_2O_4$/CuO/CdS core-shell. No previous report has used leaf extracts from Alocasiamacrorrhiza as reducing agents to create MNPs. This work studied the MET degradation reaction under solar radiation utilising MNPs immobilised on NRs. Using artificial neural networks (ANNs), the influence of pH, catalyst dose, MET concentration, and contact time was evaluated. Sensitivity analysis determined how each variable affected photocatalysis.

MATERIALS AND METHODS

Reagents and chemicals

Metronidazole ($C_6H_9N_3O_3$) with a purity of 99% was provided by Samara Company in Iraq. The physical and molecular structure of MET is shown in Table 1. The chemicals ferric chloride hexahydrate ($FeCl_36H_2O$) and cupric chloride dihydrate ($CuCl_22H_2O$) were purchased from Shanghai Macklin BioChem Technology Co. Ltd. (Shanghai, China). Oxalic acid (ethanedioic acid) was bought from Tianjin Kermel Chemical Reagent Company (Tianjin, China). All chemicals used were of analytical quality, including the copper nitrate, ferric nitrate, cadmium chloride, sodium sulfide, nitric acid, isopropanol, sodium bicarbonate, sodium carbonate, Nafion solution, and agar (R&M Marketing, Essex, UK). The analysis made use of these resources in their original form, without any modifications.

Preparation methods

Alocasiamacrorrhizos extracts

Leaves of the fresh Alocasiamacrorrhizos plant were washed in distilled water and dried at 323 K until their weight remained constant. The mixture of 70 g of dried Alocasiamacrorrhizos leaves and 1 liter of deionized water was then sealed and heated at 333 degrees for 150 minutes. Following extraction, the filtrate was placed in the fridge for later use (Liu et al., 2020).

Magnetic nanoparticles of $CuFe_2O_4$ immobilized on Ninevite rock

An extract of 150 ml of plant material mixed with 70 g of Ninevite and 0.02 mol of oxalic acid for 30 minutes at 250 rpm. A 50 mL solution of ethylene glycol (EG) was then added, along with 0.5 g of $FeCl_36H_2O$ and 0.2 g of $CuCl_{22}H_2O$. After then, 0.2 g of ammonium acetate (CH_3COONH_4) added to the mixture under rapid stirring. The

Table 1. Metronidazole's physical and chemical structures

Characteristic		Metronidazole antibiotic (MET)
Molecular formula	$C_6H_9N_3O_3$	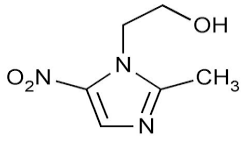
Molecular weight (g/mol)	171.2	
Water solubility (g/L)	9.5	
pK_a	2.55	
Melting point (°C)	159-163	
K_H (mol/dm^3 atm)	5.92×10^7	
Vp (Pa)	4.07×10^{-7}	

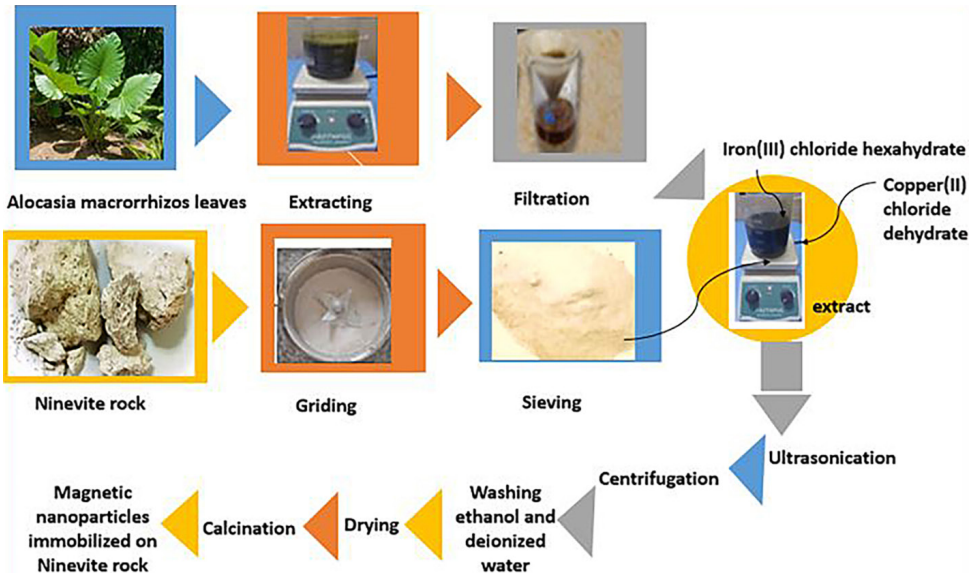

Figure 1. The synthesis stages of magnetic nanoparticles immobilized on Ninevite rock

solution was ultrasonicated for 30 minutes. The homogeneous mixture then putted into a 40 mL Teflon-lined stainless steel autoclave and heated for 20 hours at 200 °C (Massoud-Sharifi et al., 2019). Figure 1 is a diagram depicting the various stages of Magnetic nanoparticle immobilization on Ninevite rock.

Magnetic nanoparticles of $CuFe_2O_4$/CuO immobilized on Ninevite rock

Under ambient conditions, a solid powder of $CuO/CuFe_2O_4$ nanocomposite was produced utilizing an ultrasonic technique. An ultrasonic was used to sonicate 0.1 g of copper ferrite and 15 mL of ethylene glycol for 25 minutes. Then, 50 mL of DI H_2O was used to dissolve 0.12 g of copper nitrate ($Cu(NO_3)2H_2O$), which was then added gradually to the copper ferrite/EG blend. To adjust the pH to 11, 15 mL of ammonia solution (25%) was added during sonication. The product was collected by centrifugation following the sonication step and then washed in ethanol and deionized water (DI) to remove any organic compounds that had adsorption sites on the surface.

After being dried at 70 °C, the nanocomposite was placed in a crucible and calcined at 200 °C for 2 hours. (Massoud-Sharifi et al., 2019).

Magnetic nanoparticles of $CuFe_2O_4$, CuO, and CdS immobilized on Ninevite rock

This composite was created using a modified chemical process, commonly known as the bottom-up approach in nanotechnology, according to references (Massoud-Sharifi et al., 2019), (Tran Thi et al., 2021). The precursors of the CdS nanocomposite were cadmium chloride hydrate ($CdCl_2.2H_2O$) and thiourea. $CdCl_2.2H_2O$ and cadmium were dissolved in 100 ml of ethanol using an ultrasonic instrument (60 Hz, 80% R) for 15 minutes. The $CdCl_2 \cdot 2H_2O$ that was dissolved in ethanol was added drop by drop to the CdS-ethanol solution, and then 0.152 g of thiourea was added drop by drop to create a mixture. The mixture was agitated for 9 hours at 80 degrees Celsius using the reflex method to ensure that all of the chemicals were thoroughly reacted. The orange-yellow solution was filtered, rinsed with distilled water and ETOH, and dried. As-prepared $CuFe_2O_4$/CuO and CdS at a 2:1 mass ratio were suspended in ethanol to synthesize CdS-$CuFe_2O_4$CuO (25 mL). Then, the slurry was ultrasonically treated at a temperature of 80 °C until the mixture dried out. After 360 minutes in a vacuum oven at 100 degrees Celsius, the mixture was crushed using a mortar and pestle. The $CuFe_2O_4$CuO/CdS nanocomposite was created by calcining the powdered material at 400 °C for 180 minutes in a tube furnace under an N_2 atmosphere (Tarek et al. 2019).

Characterization

Magnetic nanocomposite samples were analyzed for structure and phase in the XRD Laboratory at Kashan University using an X-ray diffractometer (XRD; Phillips, Xpert, Holland) equipped with a monochromatic CuK source

(=1.541874). The surface morphology of our samples was investigated at Tehran University using scanning electron microscopy (SEM) images acquired using an SEM-EDS instrument (ARYA Electron Optic, FE-SEM). All of our samples were analyzed with a Fourier transform infrared spectrometer (also known as a Jasco) at Tehran University. These FTIR spectra were collected between 4000 and 400 cm^{-1} with a wavenumber resolution of 4 cm^{-1}. Using a vibrating sample magnetometer (PPMS6000, Quantum Design) and an applied magnetic field of up to 1 T, the magnetic characteristics of magnetic nanoparticles were determined at room temperature. From the related hysteresis loops that were collected, each sample's saturation magnetization (MS), remanent magnetization (MR), and coercivity (Hc) were calculated.

Evaluation of nanocomposite samples for photocatalytic activity

MET was used to test the photocatalytic activities of ninivite, $CuFe_2O_4$/NRs, $CuFe_2O_4$/CuO/NRs, and $CuFe_2O_4$/CuO-CdS/ NRs samples, respectively. This was done using a batch system. $CuFe_2O_4$ is easily retrieved due to its ferromagnetic characteristics. The reactor was composed of Pyrex glass (1 L) with solar irradiation reflective power (Mhemid et al., 2022), with a piece of mirror inserted at the bottom (used as a reflector). After that, several concentrations of MET solution (15, 30, and 100 mg/L) were formed, and the contents of the reactor were given a pH adjustment using diluted HCl or NaOH solution using a pH metre (model INOLAB 72, WTW Co., Weilheim, Germany). The MNCs were then added to the solution at the desired concentrations of 20, 40, and 80 mg/L. The mixture was stirred at room temperature for 30 minutes before being put on a magnetic stirrer (BOECO MSH-300N, Hamburg, Germany) at 200 rpm for 180 minutes. The first adsorption equilibrium between MET and MNCs was reached by leaving the solution in a dark place for 30 minutes. Next, 150, 250, and 500 mg/L of H_2O_2 were added. The antibiotic solution was then exposed to solar light to start the photodegradation process. The catalyst was centrifuged at 200 rpm for 15 minutes, with a sample volume of 10 mL obtained at regular intervals. At a maximum of 319 nm, a spectrophotometer (UV-Vis Spectrophotometer Perkin-Elmer 55 OSE) was used to measure how much MET was left in each sample. The following equation was used to calculate the target compound elimination efficiency:

$$RE\% = \frac{(C_o - C_t)}{C_o} \times 100 \quad (1)$$

where: RE – removal efficiency;
C_o – the starting antibiotic concentration in mg/l,
C_t – the remaining antibiotic concentration in mg/l after degradation.

Experiments with solar light photocatalysis were performed between 10:30 a.m. and 2:30 p.m. on sunny days between April and November of 2021 in Mosul University's Environmental Technology lab. Each experiment was repeated in the lab at room temperature twice to confirm reproducibility, and the standard deviation for the most common measurements was less than 5%.

Artificial neural network model

For modeling, artificial neural networks (ANNs) are effective computational tools. In instances where the evident form of the link between the different variables is unknown, their flexible nature makes them capable of finding complex non-linear correlations (Turp S.M., 2011). No additional analytical simplifications are used; instead, the outcomes of all objects are determined using a numerical simulation tool. The created dataset is then divided into a training set and a test set randomly. The training set is used to train the ANN to mimic the behavior of the parameterizable object. The ANN can forecast test data results once the training phase was already over. Finally, the results of the test data that were numerically simulated and the test data that the ANN predicted are compared. With the aid of ANNs, the objective of this strategy should be to minimize the effort of tests involving numerous identical objects (Burghardt and Garbe, 2018). The parameters that were accounted for the input and output layers are pH, radiation period, initial MET concentration, H_2O_2 concentrations, catalyst magnetic nanocomposites concentrations for input layer, and MET photocatalytic removal efficiency for the output layer.

RESULTS AND DISCUSSION

Structural characteristics and crystalline phases

The crystalline structure of $CuFe_2O_4$ powder, $CuFe_2O_4$/CuO, and $CuFe_2O_4$/CuO/CdS core-shell

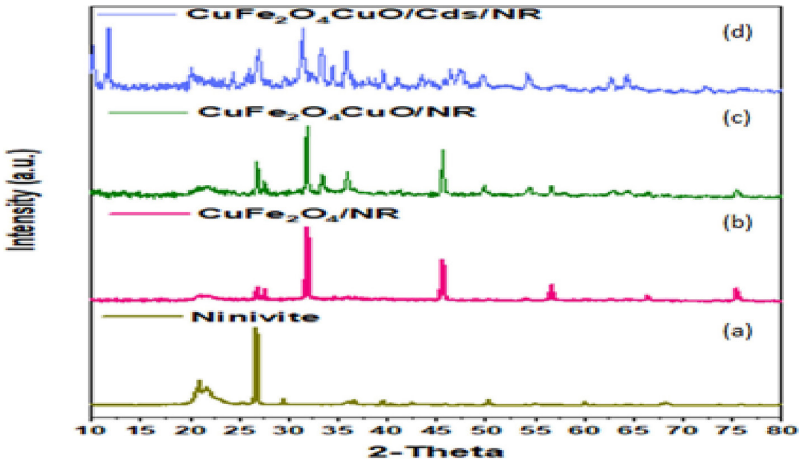

Figure 2. XRD patterns of Ninivite rock, $CuFe_2O_4$/NR, $CuFe_2O_4$/CuO/NR and $CuFe_2O_4$/CuO/CdS/NR

materials immobilized on NRs was determined by XRD analysis (Fig. 2). The crystal structure of natural, almost pure Ninivite silica rock has also been investigated with X-rays.

X-ray powder diffraction was conducted on Ninivite silica, which was used as a raw material. Figure 2 (a) shows the pattern of the sample, which has reflections that are typical of quartz as well as montmorillonite, illite, alunite, and gypsum phases (Klein et al., 1993). The X-ray pattern, which reveals the diffraction peaks at 2θ = 16° and 28°, can also be used to characterize the material.

The addition of $CuFe_2O_4$ to the Ninivite surface was investigated. No further catalytic uses of metal- or nanoparticle-decorated NRs have been reported in the literature to the best of our knowledge. Diffraction peaks can be seen at 27.4°, 31.73°, 45.45°, 56.52°, 66.32°, and 75.3° in the $CuFe_2O_4$ pattern (Fig. 2b). These diffraction peaks (space group Fd3m, JCPDS No. 34-0425) show the crystallographic planes of the $CuFe_2O_4$ cubic spinel phase (Tang et al., 2016; Gupta et al., 2020).

The magnetic composite material ($CuFe_2O_4$/CuO/NR) sample's XRD pattern, which was created by combining the calcination temperature and the ultrasonic power, is shown in Figure 2c. This pattern does not have any peaks that are distinguishable from the peaks that are typically found in copper ferrite and copper oxide. The ($CuFe_2O_4$/CuO/NR) X-ray diffraction pattern (Fig. 2c) had several intense diffraction 2 angles at 27.4°, 31.73°, 33.42°, 35.97°,45.45°,49.67°, 54.12°, 56.52°, 62.67°, 64.32°,66.32° and 75.3° demonstrating (Massoud-Sharifi et al., 2019) the existence of each component in the as-prepared nanomagnetic composite (Fig. 2c).

The XRD patterns of the synthesisedCu-Fe_2O_4/CuO/CdS/NR are shown in Figure 2d after it was subjected to analysis. This pattern shows that the diffraction peaks match well to those of as-prepared $CuFe_2O_4$@CuO and CdS, which is evidence that $CuFe_2O_4$/CuO and CdS are present in the hybridcatalyst. Diffraction peaks at24.325°, 26.375°, 27.075°, 43.475°, 52.175°, and 54.175° were matched to DB card numbers 9008862 and 1011260for the hawleyite and greenockite structures of CdS, respectively (Tarek et al., 2019). The diffraction peaks at 35.67 and 39.57 can be indexed to monoclinic CuO (111) and (220) (JCPDS card no. 65–2309). For $CuFe_2O_4$, the peak at 2θ of 35.67°, 43.37°, 57.32°, and 62.37° can be indexed to (311), (400), (511), and (440) (101) planes of cubic $CuFe_2O_4$ spinel (JCPDS card no. 77-0010)(Atarod and Safari, 2020).

Morphology

Figure 3 shows the SEM images of the core-shell samples of $CuFe_2O_4$, $CuFe_2O_4$/CuO, and $CuFe_2O_4$/CuO/CdS before the adsorption procedure. Figure 3(a1) shows that natural NRs has a rough texture due to the presence of irregular spherical aggregates.The substance had many tiny pores and multiple cavities, suggesting it could be a photocatalyst (Abdel-Maksoud, Imam, and Ramadan, 2018). The observed SEM images support the nanoscale size of the NR particles. It can be noticed that the $CuFe_2O_4$ sample has an agglomerated sphere-like structure, and the sizes of these spheres range from 40 to 150 nm (Fig. 3(a2)). Additionally, its surface density has been improved due to the uniform distribution of copper oxide nanospheres. Copper-ferrite nanospheres do not

exhibit considerable aggregation. Alternatively, rod-like particles form on the surface of NR particles in core-shell materials made from $CuFe_2O_4$ and CuO (Fig. 3(a3)). Also, the shape of the result is smoother than that of $CuFe_2O_4$ nanoparticles, but the sizes of the particles are not the same. This is because agglomerated particles of CuO can be found in some locations over the $CuFe_2O_4$ surface. The SEM images of CdS-$CuFe_2O_4$ hybrid nanoparticles are shown in Figure 3(a4), where the CdS particles are well distributed with $CuFe_2O_4$. The smooth interfaces of $CuFe_2O_4$ and CdS suggest the creation of a CdS-$CuFe_2O_4$ nanocomposite. Furthermore, CdS nanoparticles are dispersed randomly, so the surface of the $CuFe_2O_4$/CuO/CdS sample becomes rougher and more porous than the $CuFe_2O_4$/CuO surface (Fig. 3(a3)).

Micrograph Figs. 3b(1-4) show the SEM examination following the MET photodegradation process. The surface morphology in Figure 3a show more pores than those in Figure 3b, indicating that the nanocomposite has enough space for adsorption. According to Figures 3(b1, b2, b3, and b4), the natural NRsmaterial is almost the same; however, the surface of the $CuFe_2O_4$/NR, $CuFe_2O_4$/CuO/NR, and $CuFe_2O_4$/CuO/CdS/NR samples went through a significant change in texture, which may have been caused by the MET antibiotic that coated the nanocomposite surface, resulting in fewer pores.

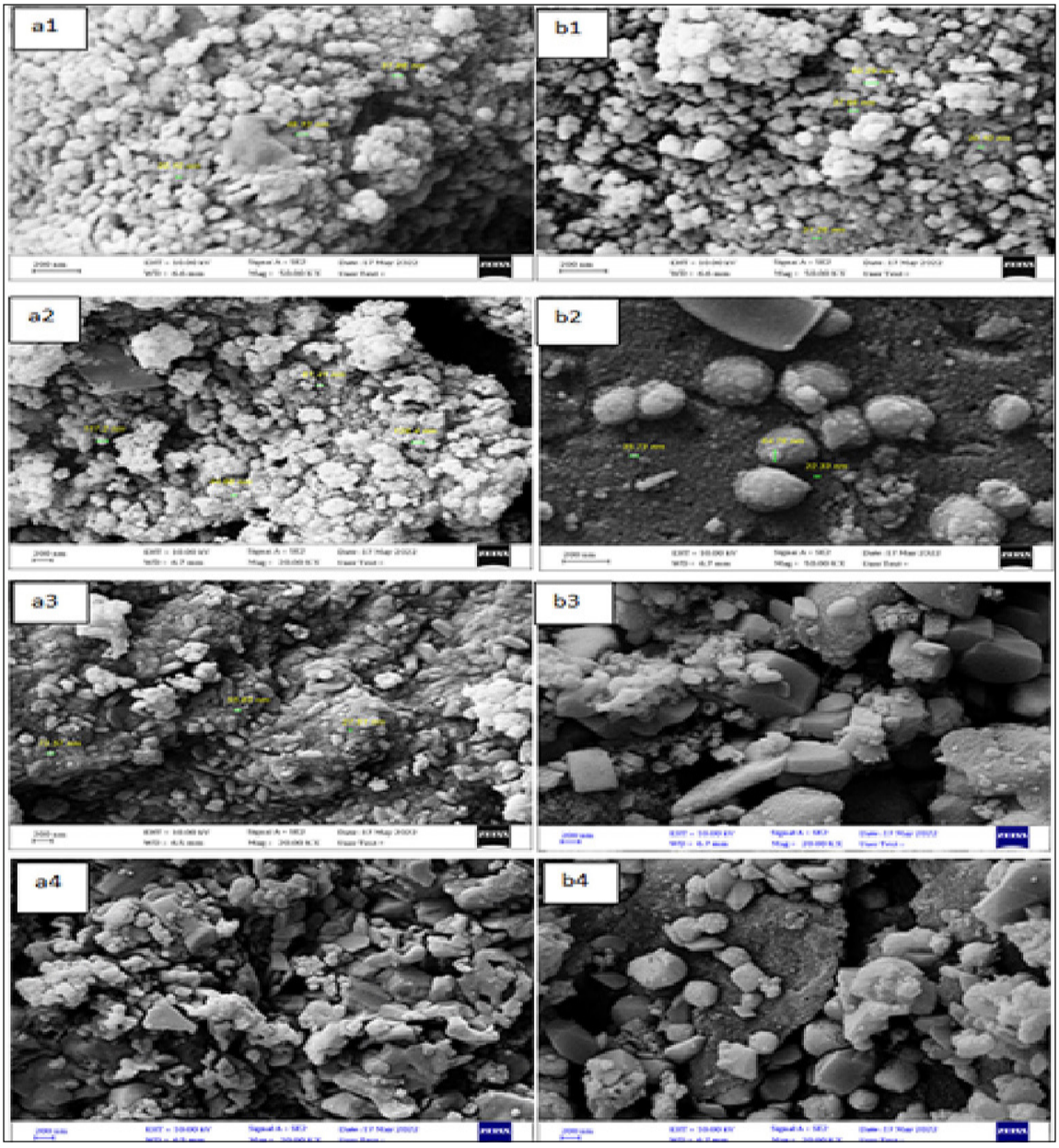

Figure 3. SEM images of the Ninivite rocks powder, $CuFe_2O_4$/NR, $CuFe_2O_4$/CuO/NR, $CuFe_2O_4$/CuO/CdS/NR (a1-4) before oxidation treatment, and after photodegradation treatment (b1-4), respectively

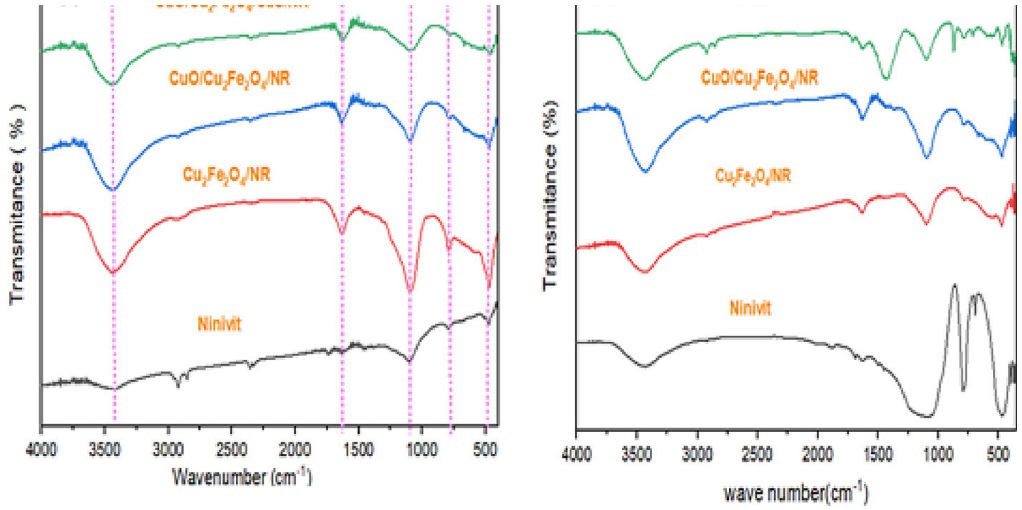

Figure 4. FTIR spectra of of Ninivite powder, $CuFe_2O_4$/NR, $CuFe_2O_4$@CuO/ NR, and $CuFe_2O_4$@CuO/CdS/ NR samples (a) before and (b) after treatment

FTIR experiments (surface functional groups)

The synthesised nanocomposites were analysed using FT-IR spectroscopy, and the results were compared to the FT-IR spectra of natural NR (Fig. 4a). The stretching vibrations of NR are unaffected by the immobilisation of $CuFe_2O_4$, $CuFe_2O_4$/CuO, or $CuFe_2O_4$/CuO/CdS nanoparticles on any of the samples, as shown by the findings of the FT-IR spectra performed on all of the samples. Several absorption bands can be seen in the spectral data, including one at 1078 cm^{-1} that is associated with the stretching vibration of Si-O (Kleni, 2007). Additionally, the Si-O-M groups are linked to 795 cm^{-1} absorption bands(Buker and Al-Botani, 2009). Absorption bands may also be visible on the surface of the material, specifically at a variation of 3642 cm^{-1}, which is indicative of

Table 2. Magnetic parameters of $CuFe_2O_4$/NR, $CuFe_2O_4$/CuO/NR, and $CuFe_2O_4$/CuO-CdS/NR samples

Sample	M_s(emu·g^{-1})	H_c(Oe)	M_R(emu·g^{-1})
$CuFe_2O_4$	32.7	146.8	4.7
$CuFe_2O_4$/CuO	124.6	97.0	26.2
$CuFe_2O_4$/CuO/CdS	121.2	97.7	29.5

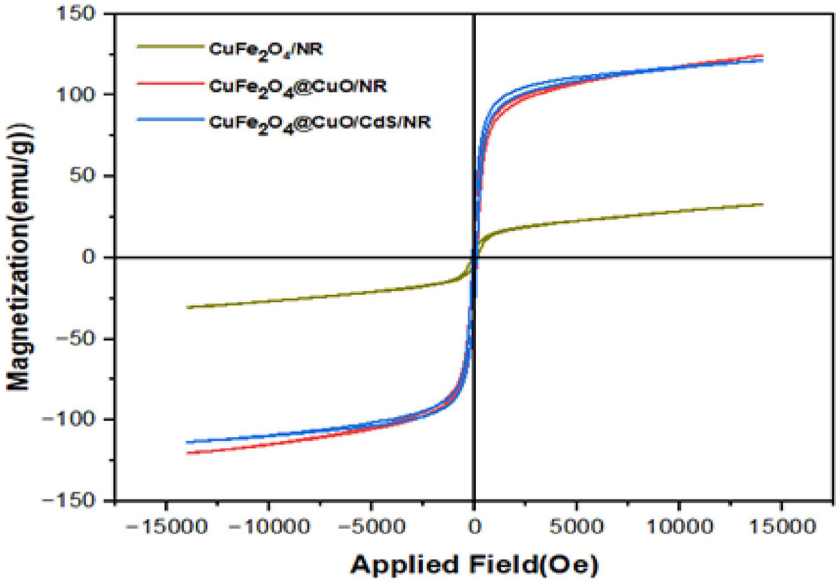

Figure 5. Magnetic hysteresis of $CuFe_2O_4$/NR, $CuFe_2O_4$/CuO/NR, and $CuFe_2O_4$/CuO-CdS/NR samples at room temperature

the O-H vibration. The 1692 cm^{-1} peaks are linked to clusters of H-O-H stretching peaks on the inner surface (Jiao et al., 2013; Tran Thi et al., 2021). The FTIR spectra (Fig. 4b) demonstrated that all of these peaks were still there after the adsorption process, indicating that the structure of the adsorbent was not altered. However, the absorption bands associated with the stretching vibration of OH groups widened and shifted to a lower wave number. The shift can be explained by the decrease in the force constant of the OH bond as a result of the hydrogen bonding between the adsorbed MET antibiotic and nanocomposites.

Magnetic properties (VSM Analysis)

The magnetic properties of the samples were investigated using a VSM withan applied magnetic field of up to 1 T (Fig. 5). The values of the samples' saturation magnetization (Ms), remnant magnetization (Mr), and coercivity field (Hc) are presented in Table 2 below. The saturation magnetization (Ms) of the $CuFe_2O_4$/NR nanocomposite is measured to be 32.7 $emu \cdot g^{-1}$, which is consistent with previous reports in the literature (Tran Thi et al., 2021). $CuFe_2O_4$/CuO/NR and $CuFe_2O_4$/CuO-CdS/NR nanocomposites are considered examples of soft magnetic materials due to their low coercivities and high saturation magnetizations. The former has a value of 124.6 $emu \cdot g^{-1}$, while the latter has a value of 121.2 $emu \cdot g^{-1}$. On the other hand, $CuFe_2O_4$ has a lower MS value and HC value. This could be because of the distribution of magnetic cations, the sintering temperature, the grain size, the chemical composition, or the density that causes major changes in their magnetic properties (Beyranvand et al., 2022).

Catalytic activity of Ninivite/ Magnetic nanocomposite

The degradation of MET in the presence of sunlight was used to assess the photo-Fenton catalytic efficacy of $CuFe_2O_4$, $CuFe_2O_4$/CuO, and $CuFe_2O_4$/CuO-CdS core-shell materials immobilized onto NRs (Table 3). Under solar irradiation, the removal efficiency rose as $CuFe_2O_4$ was substituted by $CuFe_2O_4$/CuO and $CuFe_2O_4$/CuO-CdS core-shell materials. Different parameters, such as pH, irradiation time, the initial concentration of MET, H_2O_2 concentrations, and catalyst nanocomposites concentrations in the aqueous solution, were tested to see how they affected the elimination effectiveness of the MET antibiotic that had been immobilized onto NRsusing nanomagnetic catalysts. The results showed that the elimination efficiency varied depending on the condition. The outcomes of are detailed in Table 3. The maximum capacity is found to be at pH = 3, and it is seen that the removal rate efficiency for all trials is high in acidic solutions (pH = 3), at H_2O_2 concentrations of 250 mg/L, MET concentrations of 15 mg/L, and MNC concentrations of 15 mg/L. This can be attributed to the acidity of the pH; the positively charged active sites on the MNCP's surface facilitate the absorption of the MET antibiotic (Berg et al., 2009). The adsorption capability declined dramatically when the pH changed from 3 to 11. This is because, in a slightly acidic medium, the MNCPs' surface may become less protonated by H^+ cations, resulting in a slower physical adsorption processthat is, a weaker attraction between the negatively charged pollutant molecules and the active sites of the catalyst. In addition, an increase in pH above 7 does not affect the removal value, showing that the rivalry between contaminating anions and negative OH ions (in the base medium) has no impact on the adsorption process.

The rate of decomposition is faster up to a concentration of 250 mg/L of hydrogen peroxide, but beyond that, the amount of antibiotics removed steadily decreases (Table 3). This decrease may be attributable to •OH radical scavenging as H_2O_2 concentrations exceed 250 mg/L (Cano et al., 2020).

According to Table 3, the most effective conditions for removing MET were a 20 mg/L catalyst dosage, a pH of 3, 250 mg/L H_2O_2, and a 180 min reaction time. The removal efficiency dropped as the catalyst concentration exceeded 20 mg/L. When there is a higher dose of the catalyst, the particles stick together, making it harder for light to pass through the reactor (Farzadkia et al., 2015).

Artificial neural network applications

Due to its ease of use in simulation, prediction, and modeling of process performance, artificial neural networks are utilized in many fields of science and engineering as a promising tool. The outcomes of the photocatalytic oxidation of MET are shown in Figure 6. An ANN model of synthetic effluent with MET and $CuFe_2O_4$/CuO-CdS/ NRs catalyst exposed to solar radiation with varying pH, radiation period, initial MET, H_2O_2, and catalyst MNPs concentrations was created.

Table 3. Experimental conditions of batch-scale

Ninivite (NRs)	pH*			Catalyst dose mg/L**			H_2O_2 concentration mg/L ***			MET concentration mg/L***		
Time	RE% at pH 3	RE% at pH 7	RE% at pH 11	RE% at Dose=20	RE% at Dose=40	RE% at Dose= 80	RE% at H_2O_2=150	RE% at H2O2=250	RE% at H2O2=500	RE% at Con.=15	RE% at Con.=30	RE% at Con.= 100
-30	3.23	2.10	2.00	3.23	2.62	2.42	1.93	3.23	2.13	3.23	2.90	2.10
15	6.75	5.43	4.12	6.75	5.14	4.34	5.45	6.75	5.30	6.75	6.12	5.54
30	10.25	9.50	7.40	10.25	7.71	6.95	8.75	10.25	9.07	10.25	9.83	9.39
45	18.65	18.00	12.50	18.65	17.25	16.38	16.75	18.65	17.24	18.65	17.72	16.74
60	22.54	20.54	15.12	22.54	18.94	17.74	21.14	22.54	21.23	22.54	21.81	21.17
90	25.68	24.32	21.01	25.68	21.07	20.87	24.03	25.68	24.47	25.68	25.05	24.77
120	28.74	27.23	23.43	28.74	25.53	23.23	27.21	28.74	27.43	28.74	28.01	27.13
150	31.55	30.45	27.21	31.55	26.19	24.74	30.56	31.55	28.94	29.12	28.47	28.09
180	40.67	38.90	30.31	32.11	27.50	25.98	30.97	32.00	29.32	31.55	30.67	30.45
$CuFe_2O_4$/ NRs	pH*			Catalyst Dose mg/L**			H_2O_2 concentration mg/L ***			MET concentration mg/L***		
Time	RE% at pH 3	RE% at pH 7	RE% at pH 11	RE% at Dose=20	RE% at Dose=40	RE% at Dose= 80	RE% at H2O2=150	RE% at H2O2=250	RE% at H2O2=500	RE% at Con.=15	RE% at Con.=30	RE% at Con.= 100
-30	5.32	4.14	3.25	4.23	5.32	3.54	4.17	5.32	3.49	5.32	4.54	3.25
15	7.36	6.45	5.33	6.78	7.36	5.74	5.87	7.36	5.08	7.36	6.08	5.23
30	10.44	9.54	8.98	9.25	10.44	8.44	8.45	10.44	6.25	10.44	9.72	8.37
45	14.32	12.22	10.41	12.44	14.32	10.98	11.23	14.32	9.87	14.32	13.65	12.27
60	28.36	26.35	24.25	25.23	28.36	21.25	24.15	28.36	21.74	28.36	26.98	24.17
90	40.21	35.34	31.41	33.23	40.21	30.41	30.24	40.21	28.41	40.21	38.25	36.28
120	52.38	48.52	41.23	46.21	52.38	41.23	47.21	52.38	45.21	52.38	46.87	42.18
150	63.23	60.44	55.45	60.41	63.23	57.62	56.84	63.23	52.32	63.23	58.67	52.87
180	85.32	75.23	68.41	72.23	85.32	67.23	70.23	85.32	65.24	85.32	78.23	65.23
$CuFe_2O_4$/ CuO/ NRs	pH*			Catalyst Dose mg/L**			H_2O_2 concentration mg/L ***			MET concentration mg/L***		
Time	RE% at pH 3	RE% at pH 7	RE% at pH 11	RE% at Dose=20	RE% at Dose=40	RE% at Dose= 80	RE% at H2O2=150	RE% at H2O2=250	RE% at H2O2=500	RE% at Con.=15	RE% at Con.=30	RE% at Con.= 100
-30	9.23	8.08	6.52	9.23	8.21	7.05	7.16	9.23	6.87	9.23	7.24	5.36
15	13.25	12.05	10.32	13.25	11.21	10.74	12.34	13.25	11.34	13.25	11.24	10.45
30	21.54	17.05	15.98	21.54	18.52	16.84	18.65	21.54	16.34	21.54	17.34	14.43
45	38.54	34.18	31.47	38.54	35.2	32.45	34.47	38.54	33.54	38.54	35.64	31.25
60	63.23	58.54	65.87	63.23	58.41	52.97	57.65	63.23	52.47	63.23	60.52	56.34
90	81.03	82.32	75.28	81.03	65.22	61.07	62.603	81.03	63.23	81.03	71.7	68.82
120	90.03	83.5	77	90.03	77.34	72.35	75.24	90.03	71.25	90.03	83.58	76.35
150	90.45	83.8	77.65	90.45	78.12	73.21	75.81	90.45	71.8	90.45	84	77.12
180	90.62	84	78	90.62	78.83	74.01	76.09	90.62	72.35	90.62	84.43	77.602
$CuFe_2O_4$/ CuO-CdS/ NRs	pH*			Catalyst Dose mg/L**			H_2O_2 concentration mg/L ***			MET concentration mg/L***		
Time	RE% at pH 3	RE% at pH 7	RE% at pH 11	RE% at Dose=20	RE% at Dose=40	RE% at Dose= 80	RE% at H2O2=150	RE% at H2O2=250	RE% at H2O2=500	RE% at Con.=15	RE% at Con.=30	RE% at Con.= 100
-30	11.35	10	9.54	11.35	9.45	8.52	8.52	3.49	11.35	9.57	7.37	11.35
15	20.64	18.12	16.75	20.64	13.48	11.34	8.64	11.35	20.64	14.47	12.38	20.64
30	43.28	39.4	37.25	43.28	32.97	29.35	13.64	20.64	43.28	21.26	28.74	43.28
45	65.28	63	58.24	65.28	62.14	54.67	28.67	43.28	65.28	58.85	58.74	65.28
60	85.25	80.3	74.64	85.25	75.45	69.74	50.42	65.28	85.25	70.41	66	85.25
90	95.32	91.4	84	95.32	83.00	77	78.62	85.25	95.32	83.2	68	95.32
120	95.8	92.2	85.13	95.8	84.47	89.3	80.2	95.32	95.8	83.87	70	95.8
150	97	93.12	85.7	97	85.00	90.11	82.3	95.8	97	84.16	73	97
180	97.5	93.45	86.12	97.5	85.43	90.6	82.7	97	97.5	84.76	74.24	97.5

Note: * pH (3, 7, 11), catalyst dose 20 mg/L, H_2O_2 250 concentration mg/L, MET concentration 15 mg/L, ** pH 3, catalyst dose (20, 40, 80) mg/L, H_2O_2 250 concentration mg/L, MET concentration 15 mg/L, *** pH 3, catalyst dose 20 mg/L, H_2O_2 (150, 250, 500) concentration mg/L, MET concentration 15 mg/L, **** pH 3, catalyst dose 20 mg/L, H_2O_2 250 concentration mg/L, MET concentration (15, 30, 100) mg/L.

It also shows how the results of the ANN Model and experimental adsorption may be compared. The initial concentration of MET, pH value, H_2O_2 concentrations, and catalyst MNP concentrations served as the input values for the ANN model, while the evaluation of MET oxidation magnitude served as the output value. Three hidden neurons produced superior results for the ANN models that were assessed when there were varying numbers of hidden neurons. The computing time does not decrease as the number of neurons increases. For the hidden and output layers of the ANN model, the transfer functions "Tansig" and "Purelin," respectively, were used. Time duration, pH, initial concentration MET, and catalytic dose were the input variables in the neural network forward feeding. The degrading ratio (C/Co) represented the output variable or experimental response. Mean square error (MSE) assesses the network's performance (Eq. 2):

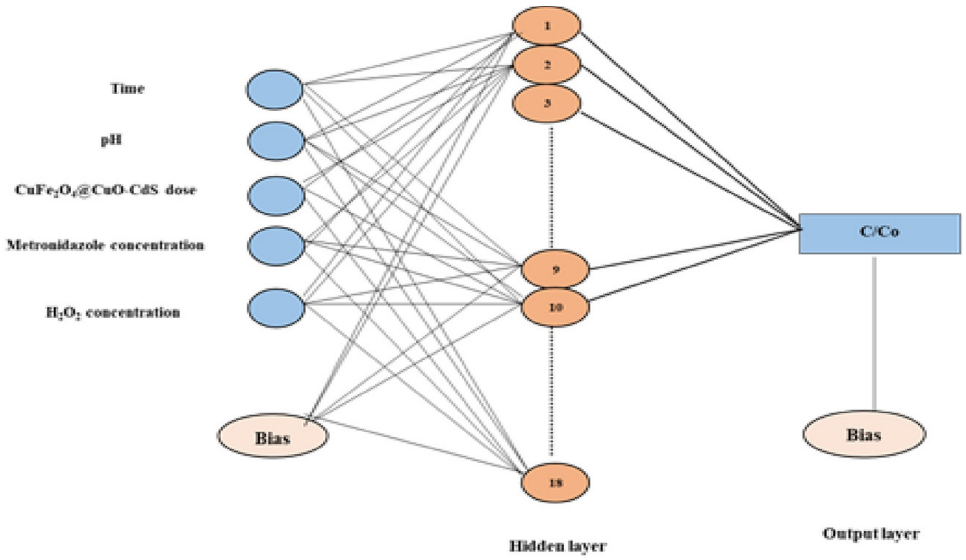

Figure 6. Optimized ANN structure

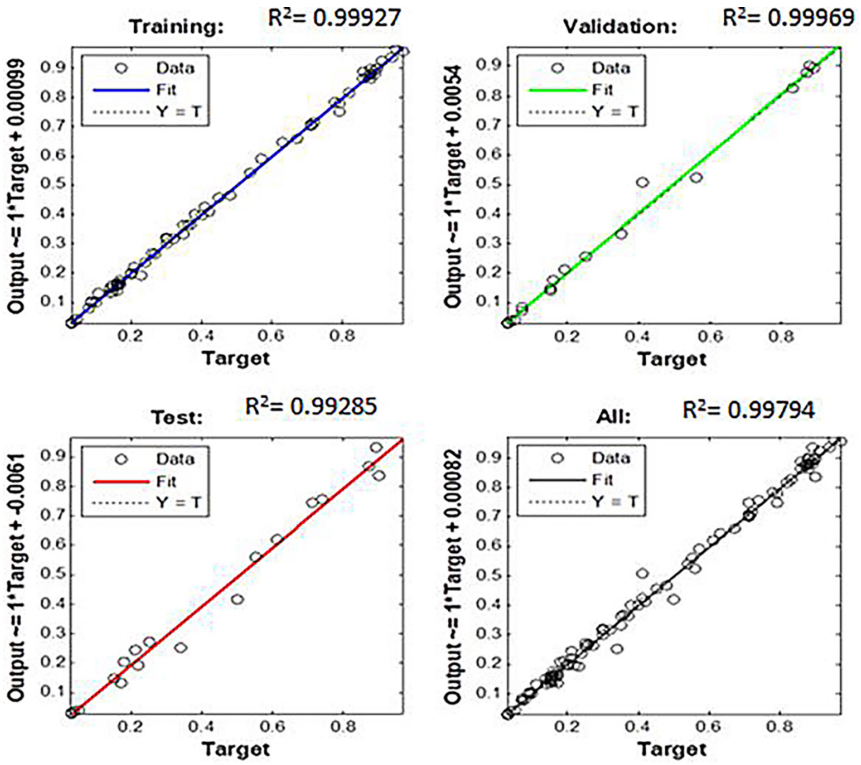

Figure 7. ANN-based linear fitting of experimental and anticipated oxidation rates

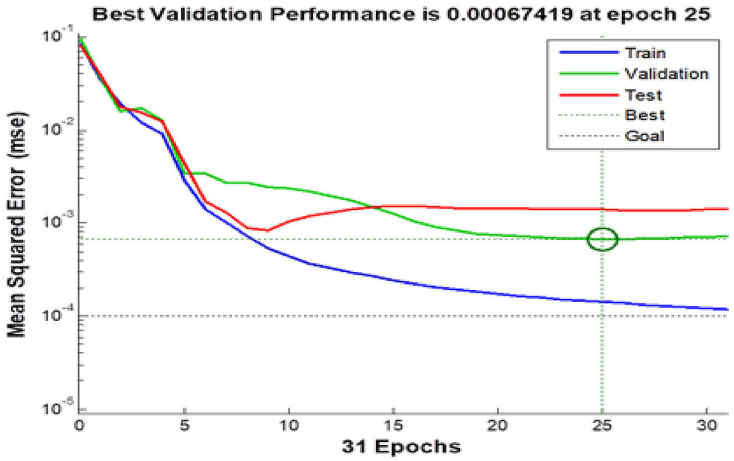

Figure 8. The performance relationship between the number of epochs and the MSE of the $CuFe_2O_4$@CuO-CdS/Ninivite prediction of the MET oxidation rate

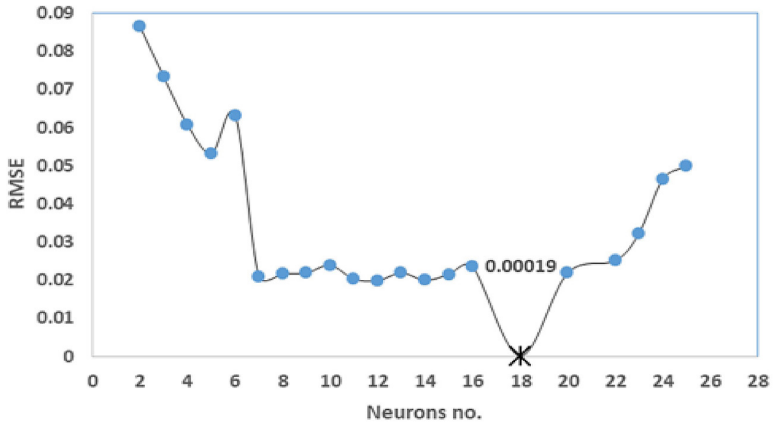

Figure 9. The relationship between the number of neurons and the root mean square error (RMSE)

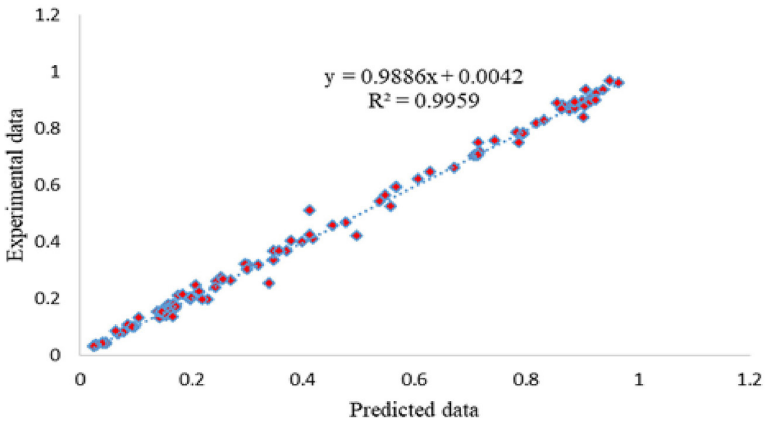

Figure 10. Comparison of the output values for the photocatalyst process between predicted and experimental values using ANN

$$MSE = \frac{\sum_{i=1}^{i=N}(Yi, perdic - Yi, \exp)^2}{N} \quad (2)$$

where: N – the number of data points,

$y_{i,predict}$ – represents the network prediction,

$y_{i,exp}$ – represents the experimental value of the i[th] datum.

In order to develop training, testing, and validation sets, the data from the 100 experimental datasets from the batch of photo degradation

tests were divided into proportions of 60%, 20%, and 20%. Different network neurons served as a stand-in for the neurons required to maintain the functional connection between inputs and outputs. A variety of topologies with different neurons ranging from 2 to 18 were examined in order to find the maximum number of hidden neurons. According to Figure 6, the optimal ANN structure for forecasting the degradation rate was chosen in the ratio 5:18:1.

As shown in Figure 7, the correlation coefficients (R^2) for the data for the training regressions, validation, testing, and for the data as a whole were 0.99927, 0.9969, 0.99285, and 0.99794, respectively.

The training was discontinued after 25 iterations, and Figure 8's validation set accuracy was 0.00067419.

According to Figure 9, which shows that the 18 hidden neurons reached the least MSE value of 0.00019, the network provided a variety of local minimum and maximum values as well as various MSE values with an increase in the number of neurons.

These findings demonstrated that the ANN model was a good and effective predictor of tests involving the photodegradation of MET antibiotics onto NMP catalyst (Fig. 10).

Since Garson suggested an equation (Eq. 3) based on the distribution of the weight of the connection, sensitivity analysis was used in the current study to determine the relevance of each input variable on the performance of the ANN model (Alwared et al., 2021). Figure 11 illustrates the relative importance of the input variables (pH, catalyst dose, H_2O_2 concentration, MET concentration, and contact time) on the rate of MET degradation from the aqueous solution. The correlation matrixes (CM) represent the weights between the hidden layers, input (CM1), and output (CM2), as shown in Equations 4 and 5.

$$Ij = \frac{\sum_{m=1}^{m=Nh}\left(\frac{w_{jm}^{ih}}{\sum_{k=1}^{Ni} w_{km}^{ih}}\right) \times W_{mn}^{ho}}{\sum_{K=1}^{k=Ni}\left\{\sum_{m=1}^{Nh}\left(w_{km}^{ih} \left| \sum_{k=1}^{Ni} W_{km}^{th}\right.\right) \times \left|W_{mn}^{ho}\right|\right\}} \quad (3)$$

where: Ij and jth – the numbers of the input and hidden neurons, respectively;
Ni and Nh – the numbers of input and hidden neurons, respectively;
Ws – the connection weights;
i, h, and o –the input, hidden, and output layers, respectively;
k, m, and n – the input, hidden, and output neurons, respectively.

$$\text{CM1} = \begin{bmatrix} Time & pH & Catalyst\ Dose & MET\ con. & H2O2\ con. \\ -0.5805 & 0.8607 & -1.8030 & -1.7325 & 0.9771 \\ -0.8612 & -1.0750 & 0.2160 & -1.0613 & 0.7889 \\ -1.7665 & -0.0884 & 2.6409 & 0.3728 & 1.3971 \\ 2.1149 & 0.8487 & -1.7496 & -0.6951 & -0.9370 \\ 0.1929 & -1.2147 & 0.1672 & -0.2593 & -2.2573 \\ 1.0827 & -1.1117 & -1.3416 & -0.2286 & -2.0755 \\ -3.2536 & 0.5441 & 0.5115 & 1.8102 & 0.4154 \\ -0.2089 & -0.1332 & -0.0109 & -2.3557 & 0.6709 \\ 1.3353 & 0.8592 & 1.2528 & -0.3595 & 1.0785 \\ -3.9353 & 0.0991 & 0.4691 & 0.6587 & -3.6358 \\ 0.5138 & 0.0791 & -0.8759 & 1.1876 & -2.2850 \\ 5.1003 & 0.1511 & 0.2824 & -0.0244 & 0.1230 \end{bmatrix} \quad (4)$$

$$\text{CM2} = \begin{bmatrix} Degradation\ rate \\ 0.9771 \\ 0.7889 \\ 1.3971 \\ -0.9370 \\ -2.2573 \\ -2.0755 \\ 0.4154 \\ 0.6709 \\ 1.0785 \\ -3.6358 \\ -2.2850 \\ 0.1230 \end{bmatrix} \quad (5)$$

Figure 11 shows that all parameters have a significant impact on the MET antibiotic's photodegradation rate. The most important parameter, having a relative relevance of 30.05%, is the dosage of $CuFe_2O_4$/CuO-CdS/NRs. Depending on the circumstances and settings, the relative relevance may vary from one researcher to the other.

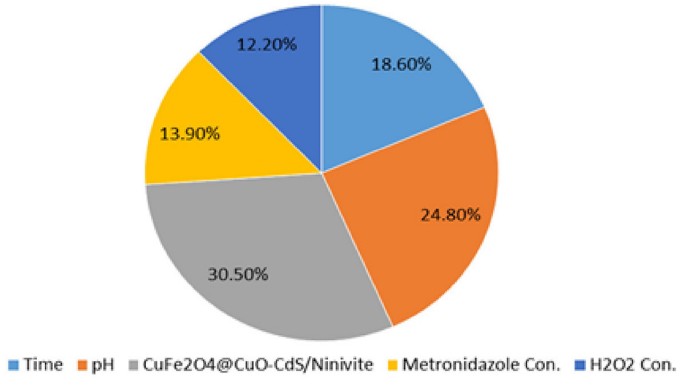

Figure 11. Pie chart showing the findings from the parameters' sensitivity analyses

CONCLUSION

In brief, using the immobilization of MNPs on the surface of Ninivite rockswere effectively created a new and efficient magnetic nanoparticle catalysts. These core-shell materials performed exceptionally performance in the degradation of MET antibiotics in a batch reactor. The best catalytic performance is demonstrated by the $CuFe_2O_4$/CuO/CdS catalyst, which may be attributed to its highest photocatalytic activity. Moreover, the core-shell catalysts were identical for practical applications since they can be easily isolated from the solution and recovered using a magnet due to the presence of magnetic $CuFe_2O_4$ cores. At optimal values of the experimental conditions, the $CuFe_2O_4$@ CuO/CdS surface was found to have a maximum MET removal rate of 97%. Based on the results of the ANN sensitivity analysis, the MNP dosage is a critical factor with a relative influence of 30.5%.

Acknowledgements

Sincere thanks go to the Environmental Engineering Lab in Mosul University for providing the authors with the tools they needed to improve the quality of this work. No funding was received for conducting this study.

REFERENCES

1. Alwared, A.I., Al-Musawi, T.J., Muhaisn, L.F., Mohammed, A.A. 2021. The biosorption of reactive red dye onto orange peel waste: a study on the isotherm and kinetic processes and sensitivity analysis using the artificial neural network approach. Environmental Science and Pollution Research, 28, 2848–2859. https://doi.org/10.1007/s11356-020-10613-6
2. Appavu, B., Thiripuranthagan, S., Ranganathan, S., Erusappan, E., Kannan, K.2018. BiVO4 /N-rGO nano composites as highly efficient visible active photocatalyst for the degradation of dyes and antibiotics in eco system. Ecotoxicology and Environmental Safety, 151, 118–126. https://doi.org/10.1016/j.ecoenv.2018.01.008
3. Atarod, M., Safari, J. 2020. Comparative Study of CuO, Fe3O4 and CuFe2O4/CuO over Montmorillonite Clay: Green Synthesis, Characterization and Catalytic Activity. ChemistrySelect, 5, 8394–8404. https://doi.org/https://doi.org/10.1002/slct.202001849
4. Berg, J.M., Romoser, A., Banerjee, N., Zebda, R., Sayes, C.M. 2009. The relationship between pH and zeta potential of ~ 30 nm metal oxide nanoparticle suspensions relevant to in vitro toxicological evaluations. Nanotoxicology, 3, 276–283.https://doi.org/10.3109/17435390903276941
5. Beyranvand, M., Zahedi, A., Gholizadeh, A. 2022. Cadmium Substitution Effect on Microstructure and Magnetic Properties of Mg-Cu-Zn Ferrites. Frontiers in Materials, 8. https://doi.org/10.3389/fmats.2021.779837
6. Buker, R.A., Al-Botani, A.S., 2009. Study of the Physical and Structural Properties of some Local Ninivites and Effect of Doping with some Chromium Complexes. J. Raf. Sci., 20, 52–64.
7. Burghardt, F., Garbe, R. 2018. Introduction of Artificial Neural Networks in EMC. In: IEEE Symposium on Electromagnetic Compatibility, Signal Integrity and Power Integrity (EMC, SI & PI), 165–169. https://doi.org/10.1109/EMCSI.2018.8495246
8. Cano, P.A., Jaramillo-Baquero, M., Zúñiga-Benítez, H., Londoño, Y.A., Peñuela, G.A. 2020. Use of simulated sunlight radiation and hydrogen peroxide in azithromycin removal from aqueous solutions: Optimization & mineralization analysis. Emerging Contaminants, 6, 53–61. https://doi.org/10.1016/j.emcon.2019.12.004
9. Fang, S., Xue, S., Wang, C., Wang, G., Wang, X., Liang, Q., Li, Z., Xu, S. 2016. Fabrication and characterization of CdS/BiVO4 nanocomposites with efficient visible light driven photocatalytic activities. Ceramics International, 42, 4421–4428. https://doi.org/10.1016/j.ceramint.2015.11.126
10. Farzadkia, M., Bazrafshan, E., Esrafili, A., Yang, J.-K., Shirzad-Siboni, M., 2015. Photocatalytic degradation of Metronidazole with illuminated TiO2 nanoparticles. Journal of Environmental Health Science and Engineering, 13, 35. https://doi.org/10.1186/s40201-015-0194-y
11. Forouzesh, M., Ebadi, A., Aghaeinejad-Meybodi, A. 2019. Degradation of metronidazole antibiotic in aqueous medium using activated carbon as a persulfate activator. Separation and Purification Technology, 210, 145–151. https://doi.org/10.1016/j.seppur.2018.07.066
12. Gupta, N.K., Ghaffari, Y., Kim, S., Bae, J., Kim, K.S., Saifuddin, M. 2020. Photocatalytic Degradation of Organic Pollutants over MFe_2O_4 (M = Co, Ni, Cu, Zn) Nanoparticles at Neutral pH. Scientific Reports, 10, 4942. https://doi.org/10.1038/s41598-020-61930-2
13. Heidari, M., Varma, R., Ahmadian, M., Pourkhosravani, M., Asadzadeh, S., Karimi, P., Khatami, M. 2019. Photo-Fenton like catalyst system: activated carbon/$CoFe_2O_4$ nanocomposite for reactive dye removal from textile wastewater. Applied Sciences, 9, 963. https://doi.org/10.3390/app9050963

14. Ingerslev, F., Toräng, L., Loke, M.L., Halling-Sorensen, B., Nyholm, N. 2001. Primary biodegradation of veterinary antibiotics in aerobic and anaerobic surface water simulation systems. Chemosphere, 44, 865–872. https://doi.org/10.1016/S0045-6535(00)00479-3
15. Jiao, H., Jiao, G., Wang, J. 2013. Preparation and Magnetic Properties of $CuFe_2O_4$ Nanoparticles. Synthesis and Reactivity in Inorganic, Metal-Organic, and Nano-Metal. Chemistry, 43, 131–134. https://doi.org/10.1080/15533174.2012.680090
16. Klein, C., Hurlbut, C.S., Dana, J.D. 1993. Manual of Mineralogy (after James D. Dana). Wiley.
17. Kleni, C. 2007. Minerals and rocks. John Wiley & Sons, Inc.
18. Liu, Q., Ma, P., Liu, P., Li, H., Han, X., Liu, L., Zou, W. 2020. Green synthesis of stable Fe,Cu oxide nanocomposites from loquat leaf extracts for removal of Norfloxacin and Ciprofloxacin. Water Science and Technology, 81, 694–708. https://doi.org/10.2166/wst.2020.152
19. Massoud-Sharifi, A., Kara, G.K., Rabbani, M. 2019. CuFe2O4@CuO: A Magnetic Composite Synthesized by Ultrasound Irradiation and Degradation of Methylene Blue on Its Surface in the Presence of Sunlight. In: The 4th International Electronic Conference on Water Sciences. MDPI, Basel Switzerland, 17. https://doi.org/10.3390/ECWS-4-06438
20. Mhemid, R.K.S., Salman, M.S., Mohammed, N.A. 2022. Comparing the efficiency of N-doped TiO_2 and commercial TiO_2 as photo catalysts for amoxicillin and ciprofloxacin photo-degradation under solar irradiation. Journal of Environmental Science and Health, Part, A 57, 813–829. https://doi.org/10.1080/10934529.2022.2117960
21. Niaki, Z.M., Ghorbani, M., Ghoreishi, S.A. 2021. Synthesis of $ZnFe_2O_4$/Uio-66 nanocomposite for the photocatalytic degradation of metronidazole antibiotic under visible light irradiation. Journal of Environmental Health Science and Engineering, 19, 1583–1596. https://doi.org/10.1007/s40201-021-00713-x
22. Nikravan, A., Afsoun. 2015. Amoxicillin And Ampicillin Removal From Wastewater by Fenton and Photo-Fenton Processes. Hacettepe University.
23. Sharma, K., Talwar, S., Verma, A.K., Choudhury, D., Mansouri, B., 2020. Innovative approach of in-situ fixed mode dual effect (photo-Fenton and photocatalysis) for ofloxacin degradation. Korean Journal of Chemical Engineering, 37, 350–357. https://doi.org/10.1007/s11814-019-0427-3
24. Shi, Y., Li, H., Wang, L., Shen, W., Chen, H. 2012. Novel α-Fe 2 O 3 /CdS Cornlike Nanorods with Enhanced Photocatalytic Performance. ACS Applied Materials & Interfaces 4, 4800–4806. https://doi.org/10.1021/am3011516
25. Sievers, M. 2011. Advanced Oxidation Processes. Treatise on Water Science 4, 377–408. https://doi.org/10.1016/B978-0-444-53199-5.00093-2
26. Sulaiman, F., Alwared, A. 2022. Ability of Response Surface methodology to optimize photocatalytic degradation of amoxicillin from aqueous solutions using immobilized TiO_2/sand. Journal of Ecological Engineering, 23, 293–304. https://doi.org/10.12911/22998993/147318
27. Tang, Y., Shih, K., Liu, C., Liao, C. 2016. Cubic and tetragonal ferrite crystal structures for copper ion immobilization in an iron-rich ceramic matrix. RSC Advances, 6, 28579–28585. https://doi.org/10.1039/C6RA00168H
28. Tarek, M., Rezaul Karim, K.M., Sarkar, S.M., Deb, A., Ong, H.R., Abdullah, H., Cheng, C.K., Rahman Khan, M.M.2019. Hetero-structure CdS–$CuFe_2O_4$ as an efficient visible light active photocatalyst for photoelectrochemical reduction of CO_2 to methanol. International Journal of Hydrogen Energy, 44, 26271–26284. https://doi.org/10.1016/j.ijhydene.2019.08.074
29. Tran Thi, T.U., Phan, V.H., Pham Nguyen, H.T., Nguyen, T.L., Vu, A.N., Le, T.K.2021. Synthesis of magnetic $CuFe_2O_4$/Fe_2O_3 core-shell materials and their application in photo-Fenton-like process with oxalic acid as a radical-producing source. Journal of Asian Ceramic Societies, 9, 1091–1102. https://doi.org/10.1080/21870764.2021.1939241
30. Turp S.M., E.B., A.A. 2011. Prediction of adsorption efficiency for the removal of nickel(ii) ions by zeolite using artificial neural network(ANN). Fresenius Environmental Bulletin, 20, 3158–3165.
31. Verma, A., Jaihindh, D.P., Fu, Y.-P. 2019. Photocatalytic 4-nitrophenol degradation and oxygen evolution reaction in CuO/g-C_3N_4 composites prepared by deep eutectic solvent-assisted chlorine doping. Dalton Transactions, 48, 8594–8610. https://doi.org/10.1039/C9DT01046G
32. Wang, X., Du, Y., Ma, J. 2016. Novel synthesis of carbon spheres supported nanoscale zero-valent iron for removal of metronidazole. Applied Surface Science, 390, 50–59. https://doi.org/10.1016/j.apsusc.2016.08.027